PAPER • OPEN ACCESS

Evaluation and optimization of geometry parameters of GAGG scintillator-based Compton Camera for medical imaging by Monte Carlo simulation

To cite this article: H. Zarei *et al* 2023 *JINST* **18** P01035

Jinst

Published by IOP Publishing for Sissa Medialab

Received: *October 26, 2022*
Revised: *December 25, 2022*
Accepted: *January 11, 2023*
Published: *January 27, 2023*

Evaluation and optimization of geometry parameters of GAGG scintillator-based Compton Camera for medical imaging by Monte Carlo simulation

H. Zarei,[a,b] **S. Razaghi,**[c] **Y. Nagao,**[d] **M. Itoh,**[a] **M. Yamaguchi,**[d] **N. Kawachi,**[d] **M.R. Ay**[b,e] **and H. Watabe**[a,*]

[a] *Cyclotron and Radioisotope Center, Tohoku University, 6-3 Aoba, Aramaki, Aoba-ku, Sendai, Miyagi 980-8578, Japan*
[b] *Research Center for Molecular and Cellular Imaging, Advanced Medical Technologies and Equipment Institute, Tehran University of Medical Sciences, Tehran, Iran*
[c] *Department of Energy Engineering and Physics, Amirkabir University of Technology, 424 Hafez Ave, Tehran, Iran*
[d] *Takasaki Advanced Radiation Research Institute, National Institutes for Quantum Science and Technology, 1233 Watanuki, Takasaki, Gunma 370-1292, Japan*
[e] *Department of Medical Physics and Biomedical Engineering, School of Medicine, Tehran University of Medical Sciences, Tehran, Iran*

E-mail: hwatabe@tohoku.ac.jp

Abstract: In nuclear medicine, the development of portable imaging devices that provide high imaging resolution and sensitivity, capable of imaging gamma rays with a wide energy range and multiple radioisotopes tracing capabilities, is so important. These goals have been possible thanks to developing a compact Compton camera, a collimatorless detector coupled to compact silicon photomultiplier(SiPM) array, using scintillator crystal. In this study, the portable segmented GAGG:Ce scintillator-based Compton camera (CC) is optimized with the GATE, a Monte Carlo simulation toolkit based on Geant4, to maximize its performance for a wide range of gamma-ray energy (364–1000 keV). The geometrical parameters are selected as optimization parameters to investigate their effects on CC's performance, including imaging resolution and absolute detection efficiency (DE_a). The geometry parameters of CC include the planner area of scatterer and absorber detectors, their thicknesses, and the distance between them. The results for the energy range of 364–1000 keV show that the most important contributions to the spatial resolution and DE_a of the camera are SAD (scatterer to absorber distance) and the scatterer area while changing absorber

*Corresponding author.

https://doi.org/10.1088/1748-0221/18/01/P01035

2023 JINST 18 P01035

area (A_A) showed the most negligible impact. In the short SADs, imaging resolution and DE_a are significantly affected by the detector's size and thickness. On the other hand, in the long SADs (> 4 cm), both spatial resolution and DE_a are significantly affected by the detector's area but less affected by the detector's thickness. Decreasing the scatterer's thickness and the absorber's size or thickness improves imaging resolution without significantly reducing DE_a. The simulation study's findings presented here will provide valuable guidelines for researchers choosing a desired CC's design according to particular objectives, manufacturing limitations in scintillator growth, cost, etc.

KEYWORDS: Portable imaging devices; Compton Camera; GAGG:Ce scintillator; Geometry parameters

2023 JINST 18 P01035

Contents

2023 JINST 18 P01035

1 Introduction

Recently, in nuclear medicine, the development of portable systems for medical imaging aimed at providing high spatial resolution has attracted much attention among researchers and manufacturers [2, 3]. The small-size imaging system, moving around the organ and providing a high-resolution image quickly, can significantly benefit diagnostic and therapeutic applications [3]. On the other hand,multi-tracer imaging can provide useful information simultaneously in the detection of a number of physiologic and pathologic functions by using radioisotope-labeled multitracers and a system that provides simultaneous imaging is necessary [4, 5].

The standard imaging systems, i.e., PET and SPECT scanners, regarding the bulky, heavy, and strictly limited gamma energy, do not meet the goals [6, 7].The integration of PET and SPECT is difficult because a conventional SPECT scanner requires a collimator and their resolutions are substantially different. So simultaneous imaging with nuclides for PET and SPECT is not obtainable [4]. These goals have been possible thanks to developing a compact Compton camera, a collimatorless scintillator crystal-based detector coupled to compact SiPM, as a promising technique for future molecular imaging [4, 8, 9]. Recently, a segmented GAGG:Ce scintillator has attracted the researcher's attention in developing a portable Compton camera due to its excellent characteristics [8, 9]. The scintillator is characterized by high light output (50000 ph/MeV), good energy resolution of around 4% (FWHM) for 662 keV gamma ray [11], and fast decay time constant of the light pulse around 100 ns [12]. Furthermore, it is a high density (6.5 g/cm^3) and non-hygroscopic

crystal without any radioactive elements in its structure and emission maximum (530 nm) suitable for silicon-based photo-detectors [11–13].

Our group designed two prototypes of SiPM- GAGG:Ce Scintillator Compton Cameras in different geometrical configurations. Both prototypes showed imaging resolution of 5 mm by MLEM algorithm for 511 keV gamma ray without any non-optimized setup [14, 15]. Extensive research has been conducted on the application of the GAGG:Ce scintillator-based Compton camera as a nuclear medicine imaging device [8] in vivo imaging [6], multiple-gamma coincidence imaging [16], intraoperative imaging [17] and monitoring of particle therapy (proton therapy and heavy-ion therapy) [18, 19] and internal radiotherapy [20, 21].

A compact GAGG:Ce scintillator-based high-resolution Compton camera was developed for molecular imaging by Kishimoto et al., and they successfully obtained a 3-D multi-color image of a live mouse in just 2 h as pre-clinical evaluation with an excellent spatial resolution of about 3.1 mm at 511 and 662 keV [6]. Compton camera-based probe with a GAGG:Ce scintillator was developed for real-time radiation-guided surgery. They demonstrated the proposed system's effectiveness with an imaging resolution of 32.5 mm [17]. A novel PET-Compton hybrid simultaneous imager based on high-pixel-resolution GAGG:Ce scintillator/SiPMs (MPPC) array was developed for multi-nuclide imaging of PET and SPECT tracers such as ^{18}F-FDG and ^{111}In, respectively [11, 12].The study aims to explore the effect of the different geometrical configurations of the segmented GAGG scintillator-based two-layer CC on its performance, including imaging resolution and absolute detection efficiency (DE_a) for a wide range of gamma-ray energy (364–1000 keV). For these purposes, we performed Monte Carlo simulations. So, the simulation study's results presented here provide an initial estimation of the appropriate CC detector size for different medical imaging applications before the practical development of the CC setup. The geometry parameters of CC include the planner area of scatterer and absorber detectors, their thicknesses, and the distance between them. The detector sizes of CC considered in this study are set as small as to provide a suitable portable imaging system.

2 Materials and methods

The GATE v9.0, a Monte Carlo simulation toolkit based on Geant4 [23], was used to model the portable CC structure and analyze the effect of each geometry factor on the DE_a and image resolution of the CC. GATE code offers the simple and easy modeling of different CC configurations user-friendly based on macro language. The CCMod actor in the GATE code is applied in our simulations [24, 25]. The CC head considered in this study (figure 1) comprised two plane-type pixelated scintillator detectors: a scatterer and an absorber. The scatterer and the absorber are GAGG:Ce scintillators with a density of 6.5 g/cm^3 [26]. The pixel area of each GAGG pixel is 0.85×0.85 mm^2 with a 0.1-mm pitch, as reported in our previous work that can provide a sub-millimeter intrinsic spatial resolution of CC. The scatterer' and absorber' area (S_A and A_A) and scatterer' and absorber' thickness (S_T and A_T), and scatterer-absorber distance (SAD) are variable geometrical parameters to optimize the Compton camera's performance.

The simulations were simplified by omitting the insensitive components of the CC prototype, i.e., crystal reflector, crystal holder, SiPM arrays, and electronic board. The camera was simulated in the box's volume filled with air, so the mentioned insensitive components are substituted by air.

2023 JINST 18 P01035

Option 4 of the standard electromagnetic physics list (emstandard_opt4), including the Doppler broadening effect, was selected. This list models physics from 0 to 100 TeV for gamma, e^- and e^+. The Klein-Nishina model implements Compton scattering. Photoelectric effect and Rayleigh scattering are both applied by the Livermore models. EM Opt4 is the best set of electromagnetic physics models selected from the low-energy and standard packages [27]. The cut values for gamma-ray and the produced electrons for all geometries (scatterer, absorber and reflectors) were set at 0.01 mm, matching one order magnitude less than their dimension [24, 25]. The point source with mono energy of 364, 511, 662, and 1000 keV was defined for I-131, Cs-137,F-18, and a high energy gamma-ray emitter as an example, respectively, with a 3 cm distance away from the center of the detector. In all studies, the intrinsic spatial blurring was defined as an ideal value by 1 mm FWHM close to pixel size. Our previous work described the scatterer and absorber's energy resolution as 18%, 16%, 14%, and 10% for energies 364, 511, 662, and 1000 keV, respectively [15]. No energy threshold for detectors was defined. Two outputs, including singles and coincidences, are produced in ASCII and Root formats [28]. The single-mode acquires the incident gamma photons detected only by the scatterer or the absorber layer. In contrast, the coincidence mode collects the incident gamma photons detected by the scatterer and the absorber layers. The single events in the scatterer and absorber layers of CC were sorted into coincidences by applying a 160 ns time coincidence window.

The DE_a and image resolution characterize the performance of the Compton camera as a function of geometry parameters as variables, including scatterer and absorber area, scatterer and absorber thickness, and scatterer-absorber distance. In each study, one geometry parameter was a variable, and other parameters were constant in all simulations.

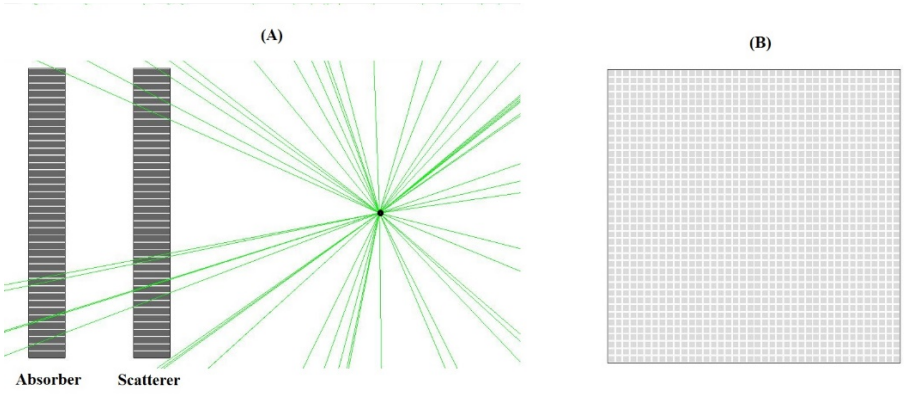

Figure 1. (A) a schematic side view and (B) a top view of the segmented GAGG scintillator-based two-layer Compton camera head.

2.1 DE_a, data processing, and image reconstruction

The DE_a was calculated as the CC's ratio of detected coincidence events regardless of energy deposition value to all gamma-rays emitted by the isotropic source.

The programs used in our previous work [14], mainly written in C++ using ROOT [29] libraries, were used to process the data after acquisition by simulation, including data selection and image reconstruction.

2023 JINST 18 P01035

After the simulation, the energy window in summation of energy in the scatterer (E_1) and absorber (E_2) for one incident photon within the range of energy resolution (ΔEFWHM) was applied to extract desirable coincidence events. The energy window was set at ±9% based on the measured energy resolution of the CC in our previous work: 364 ± 33 keV, 511 ± 46 keV and 662 ± 60 keV, and 1000 ± 90 keV. In addition, to eliminate back-scattering events, where the incident gamma rays are scattered at the absorber and photoelectrically absorbed at the scatterer, the deposited energy at the scatterer was limited as $E1 < E/(1 + 2E/mec^2)$, where E is the initial energy of the incident gamma ray. Energy windows for the absorber are not defined in this study [15]. The selected coincidence events were used to obtain image reconstruction of the point source using a simple BP (back-projection) algorithm. An elaborated description of the implementation of the BP algorithm can be found in our previous work [14]. A 128 mm×128 mm with a pixel size of 4 mm×4 mm was used for all images reconstructed.

2.2 The design of CC's geometrical optimization

The GATE simulation was performed by varying the following geometric parameters: absorber area (A_A) vs. scatterer area (S_A), SAD vs. detector area, absorber thickness (A_T) vs. scatterer thickness (S_T), and SAD vs. detector area. The DE_a and imaging resolution were computed for the four energies under these conditions.

3 Results

3.1 Geometric variable parameter: S_A and A_A, constant parameters: S_T and A_T, and SAD

Figures 2 and 3 show the influence of the S_A and A_A (cm^2) on the spatial resolution (FWHM) and the DE_a (%) of the camera. The detector's width is equal to its length in the study, and the S_T and A_T were 5 mm. To avoid the scape of scattered photon from scatterer's edge and adsorbe them by absorber effectively, the scatterer area, which is greater than the absorber area, was ignored.The scatterer and absorber cross sections are square and the $A_A \geq S_A$

The spatial resolution was increased by increasing the S_A for a particular A_A. In contrast, it was nearly constant by increasing the A_A in the constant S_A. Unlike the S_A parameter, the spatial resolution of CC was almost independent of A_A. These differences are due to differences at the subtended angles by the scatterer and absorber. When S_A increases, the solid angle of incident photons subtended by the scatterer from the source as the predominant effect, and the scattering angle of scattered photons subtended by the absorber from the scatterer increases. So the opening angle of the cone for these events is greater, and cones with increasing lengths are overlapped and constructed on the back projection. In other words, the scattering angles increase by increasing the S_A and the contribution of overlapped cones while larger opening angles increase. Finally, the widening of distributions on the back projection is increased.

The subtended angles by absorber from scatterer are in limited distribution compared to scatterer from source, so this distribution is more limited as gamma energy increases (Klein-Nishina formula) [30]. So, increasing the solid angles subtended by the absorber is not so significant by A_A increment to degrade the spatial resolution significantly. For example, the Angular distribution of Compton scattered 1000 keV is almost around $-\pi/4$–$\pi/4$ according to the Klein-Nishina formula [31].

In addition to geometrical factors, two different parameters compete to influence spatial resolution: energy resolution and the number of events participating in the image reconstruction

2023 JINST 18 P01035

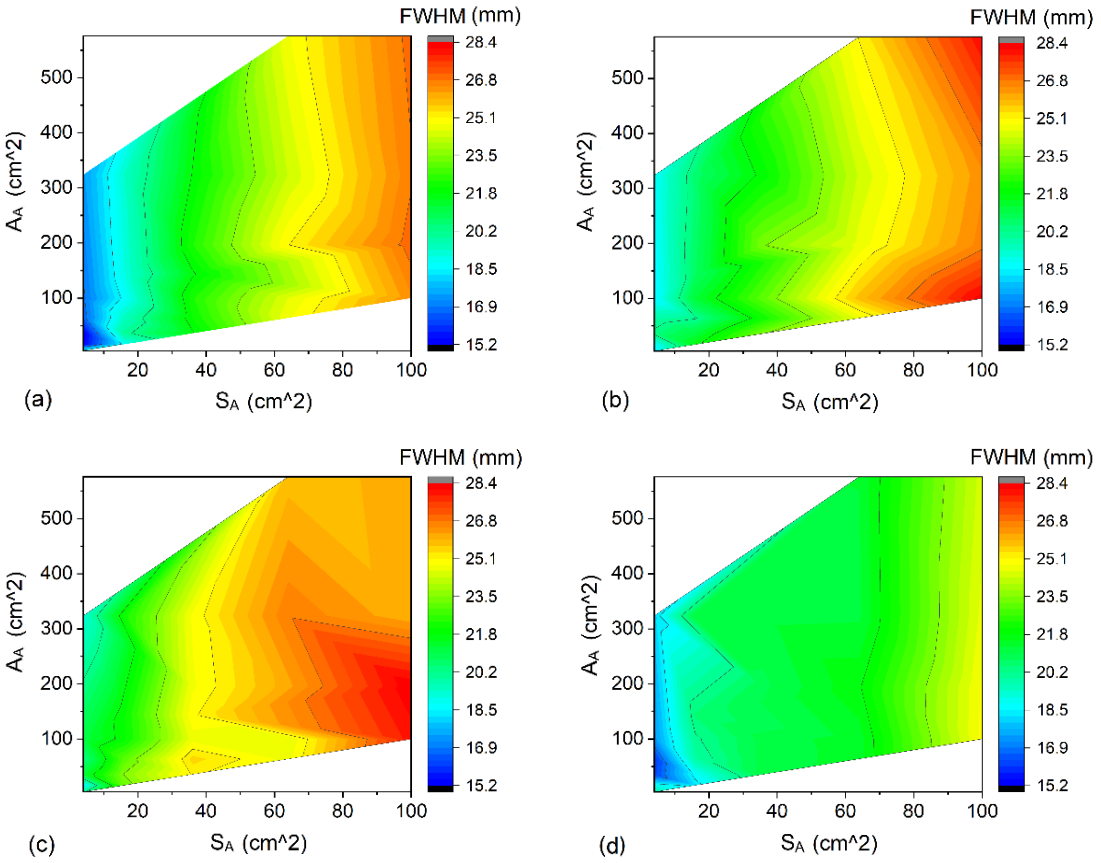

Figure 2. Spatial resolution as a function of the scatterer area (S_A) and absorber area (A_A) (cm^2) for (a) 364, (b) 511, (c) 662, and (d) 1000 keV gamma-ray source from the upper left to the lower right. In the study, the detector width equals its length, and the scatterer and absorber thickness are 5 mm. The S_A and A_A pitch is 2 cm for each side of the square area and the $A_A >= S_A$. For a constant S_A, the lower value of the A_A is equal to S_A and the upper value is 8 pitches ($2 \times 8 = 16$ cm) larger than the A_A lower value.

process. By radiation energy increment, energy resolution gets better, as mentioned in materials and methods. But the number of true coincidences decreases due to the lower number of photons participating in the image reconstruction process. For energy $\leq$ 661 keV, spatial resolution is mainly affected by the second parameter compared with 1000 keV and results in the worst spatial resolution (FWHM) for 661 keV. On the other hand, for 1000 keV radiation, spatial resolution is more effective than the number of true coincidences because of significant improvement in energy resolution. It neutralizes a lower number of actual coincidences effect.

The detection efficiency (DE$_a$) also emphasizes this issue. Figure 3 shows that the detection efficiency increases by increasing the S_A and A_A but decreases by increasing radiation energy. Therefore, fewer photons participate in image reconstruction and the spatial resolution worsens.

The DE$_a$ was grown by increasing both S_A and A_A. More photons emitted by the isotropic source and more Compton photons scattered by the scatterer detector impinge on the larger scatterer and absorber, respectively. In contrast, they escape in smaller ones without interaction. The scatterer's width on the detection efficiency is significantly more pronounced than the influence of

2023 JINST 18 P01035

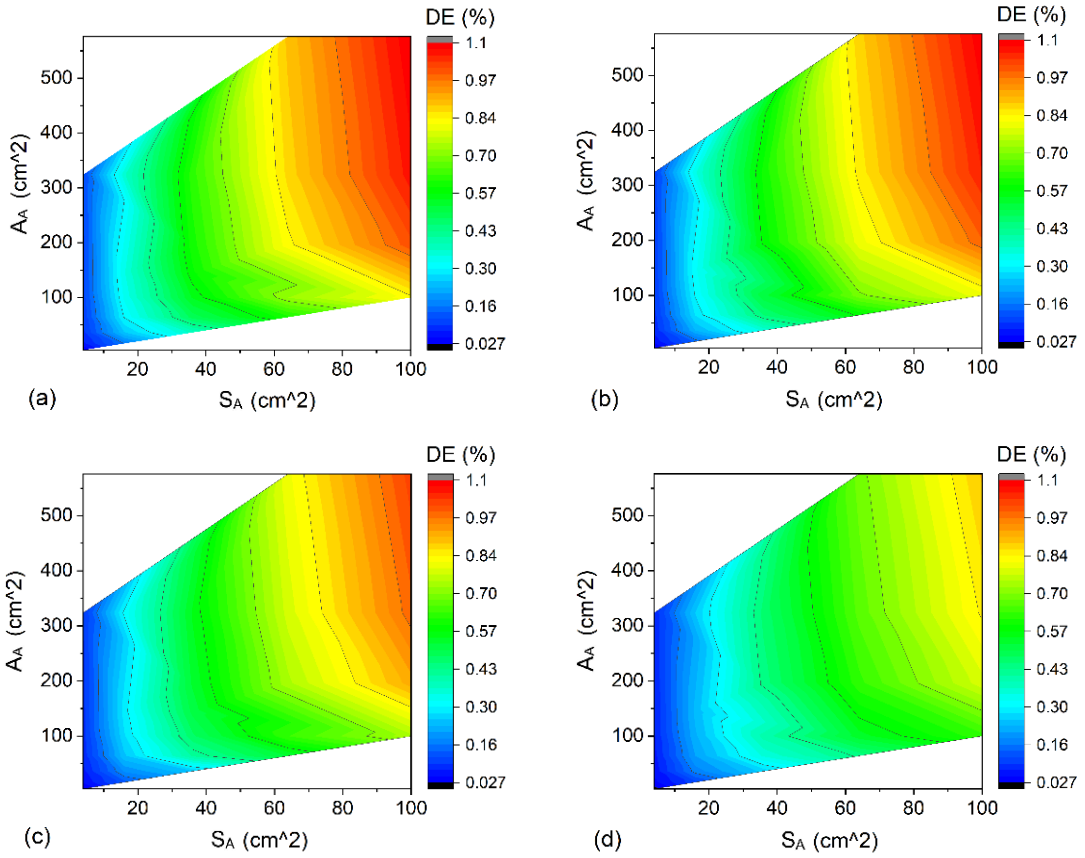

Figure 3. DE$_a$ (%) as a function of scatterer area (S_A) and absorber area (A_A) (cm^2) for (a) 364, (b) 511, (c) 662, and (d) 1000 keV gamma-ray sources from the upper left to the lower right. The condition is the same as what is mentioned in figure 2.

the absorber's width. It is because the angle of the emitted photon of the isotropic source is in all directions, unlike the angles of scattered photons from the scatterer with limited range, as mentioned above. So, more photons are impinged by enlarging the scatter area in the same gain of absorber area.

3.2 Geometric variable parameter: S_A, A_A, and SAD, constant parameters: S_T and A_T

Figures 4 and 5 show the influence of the SAD and detector Area (S_A and A_A) on the spatial resolution (FWHM) and DE$_a$ (%) of the camera. In this study, the S_A and A_A are equal (their width equals their length). The spatial resolution shows the same trends for all studied energies. It was improved with increasing SAD in a constant detector area ($S_A = A_A$) due to reducing parallax error and subsequently forming the cones with less uncertainty on axes direction in the BP plane [32]. The trend of spatial resolution also indicated its degradation with increasing the detector area in a constant SAD due to overlapping cones with increasing lengths constructed on the back projection.

The DE$_a$ grows by increasing CC area (S_A and A_A). More photons emitted by the isotropic source and more scattered photons by the scatterer detector impinge on larger scatterer and absorber, respectively, whereas they escape in smaller ones without interaction. SAD increment significantly impacted DE$_a$ at the large detector's area ($> 4\,\text{cm} \times 4\,\text{cm}$), which was negligible in the small

2023 JINST 18 P01035

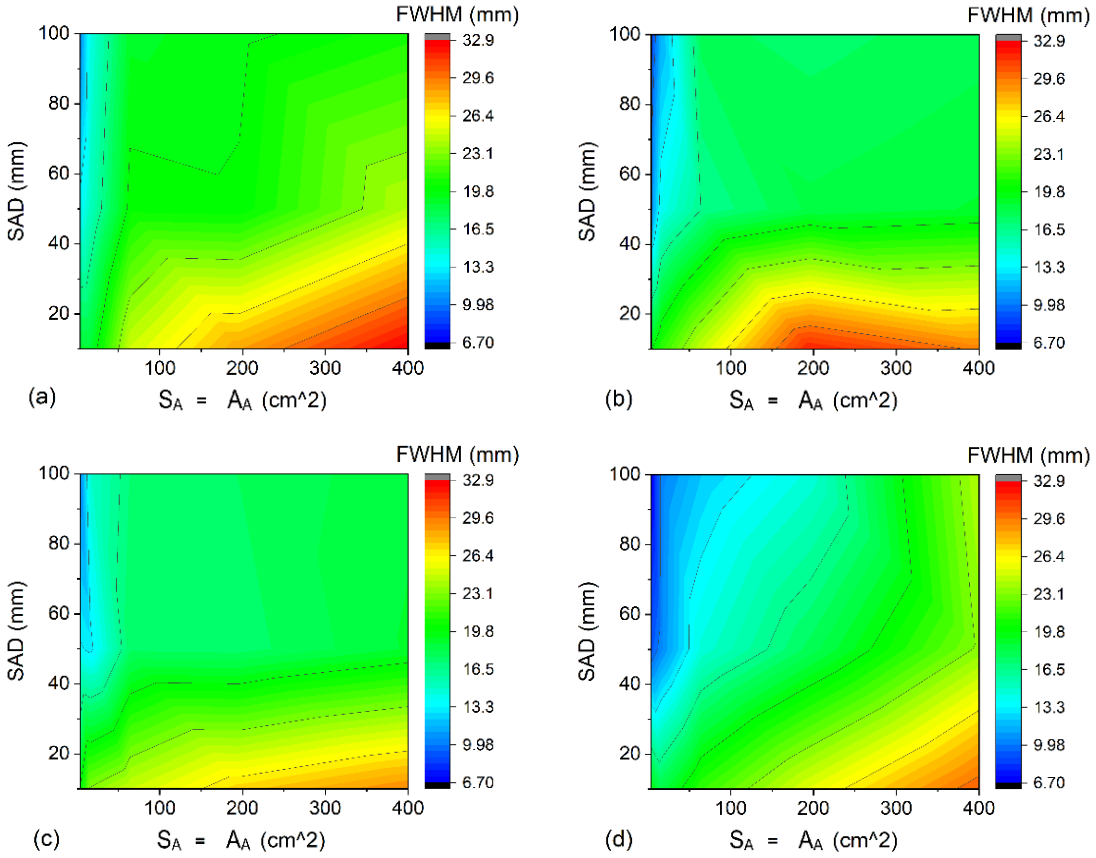

Figure 4. Spatial resolution (FWHM) as a function of scatterer-absorber distance (SAD) and detector area (cm^2) for (a) 364, (b) 511, (c) 662, and (d) 1000 keV gamma-ray source from the upper left to the lower right, respectively. The detector's width is equal to its length in the study, and the scatterer and absorber thickness are 5 mm. S_A and A_A are equal and the pitch is not constant. The area was considered to be 2×2, 4×4, 8×8, 16×16 and $20 \times 20\,cm^2$. The SAD was considered to be 10, 50 and 100 mm.

detector's area. This phenomenon is due to the difference in the range of Compton photons impinging on the absorber. In the case of a large detector area, the higher number of Compton photons with a greater scattering angle striking on the absorber detector's edge scape significantly by a SAD increment. In contrast, in small ones, the scattering angle range of Compton photons impinging on the absorber was not wide, so such phenomena were negligible.

3.3 Geometric variable parameter: S_T and A_T, constant parameters: S_A, A_A, and SAD

Figure 6 and 7 show the influence of the scatterer and absorber detector thickness (S_T and A_T) on the camera's spatial resolution and DE_a (%), respectively. In this section, S_A and A_A were considered as constant sizes of $8 \cdot 8\,cm^2$ and $10 \cdot 10\,cm^2$, respectively. We chose medium size among all studied areas in section 3.1 for three reasons: (I) to be suitable for preclinical or intraoperative imaging applications such as detector areas, (II) to cover the scattered gamma rays effectively from the scatterer by setting $S_A < A_A$ and (III) to reduce the running time of the simulation compared to large sizes.

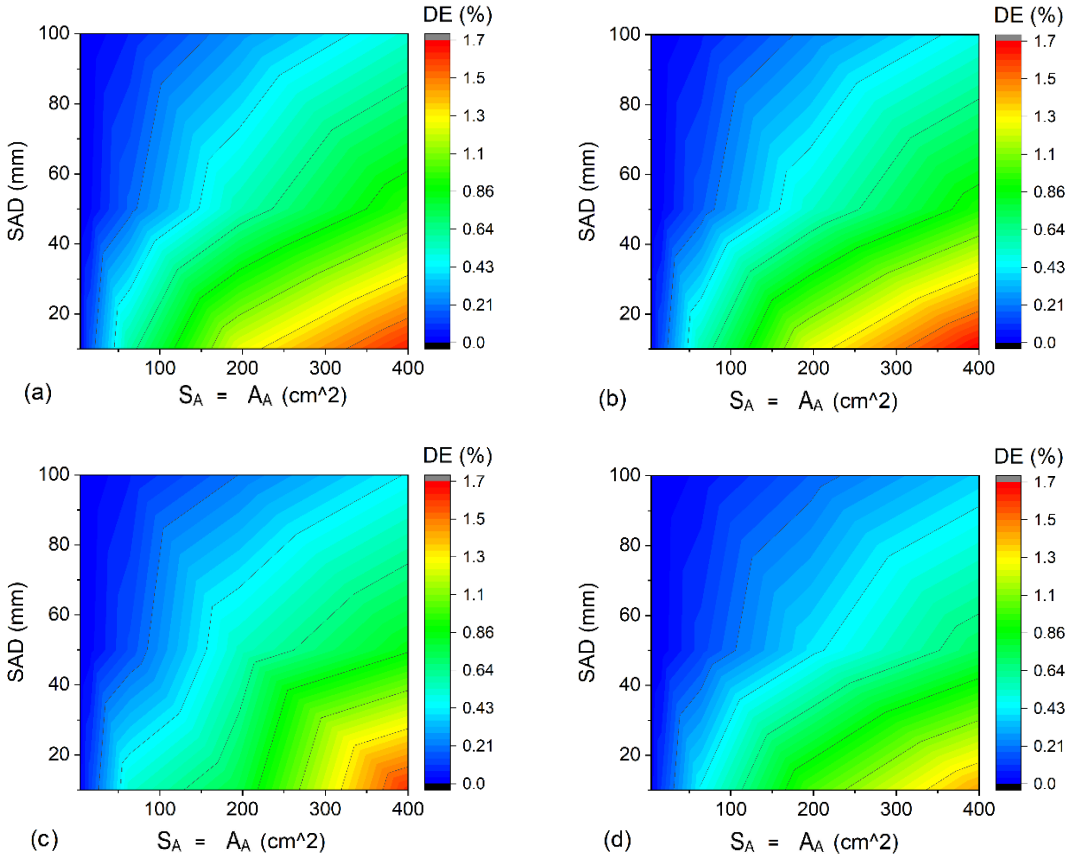

Figure 5. DE$_a$ (%) as a function of scatterer- absorber distance (SAD) and detector area (cm^2) for (a) 364, (b) 511, (c) 662, and (d) 1000 keV gamma-ray source from the upper left to the lower right, respectively. The condition is the same as what is mentioned in figure 4.

The thickness of detectors can affect the detection efficiency and imaging resolution as they can change the interaction probability and position uncertainty, respectively. The spatial resolution follows almost the same trend (pattern) by changing the detector thickness. The spatial resolution is increased by increasing the scatterer and absorber thickness. Detector thickness increment increases the parallax error due to increasing interaction uncertainty in depth [33].

On the other hand, the probability of multiple Compton scattering and backscattering increases by increasing the S_T and A_T, respectively, resulting in interaction position error of incident photon followed by degradation of image resolution. The lower the multiple scatters, the better the spatial resolution. The most noticeable change in spatial resolution was shown in high scatterer thickness by increasing the absorber thickness. It may be due to the effect of multiple Compton scattering of incident photons in the scatterer. Subsequently, a significant reduction in the number of scattered photons statically is more dominant than position uncertainty induced by increased A_T.

As A_T increases from 2 to 26 mm, the DE$_a$ grows as expected from the exponential attenuation law. For a certain A_T, the DE$_a$ grows at the beginning and then declines as the scatterer thickness (S_T) is increased. The pattern is the same from low to high A_T. In this case, the probability of Compton interaction is increased by increasing the S_T for incident photon so that the likelihood

2023 JINST 18 P01035

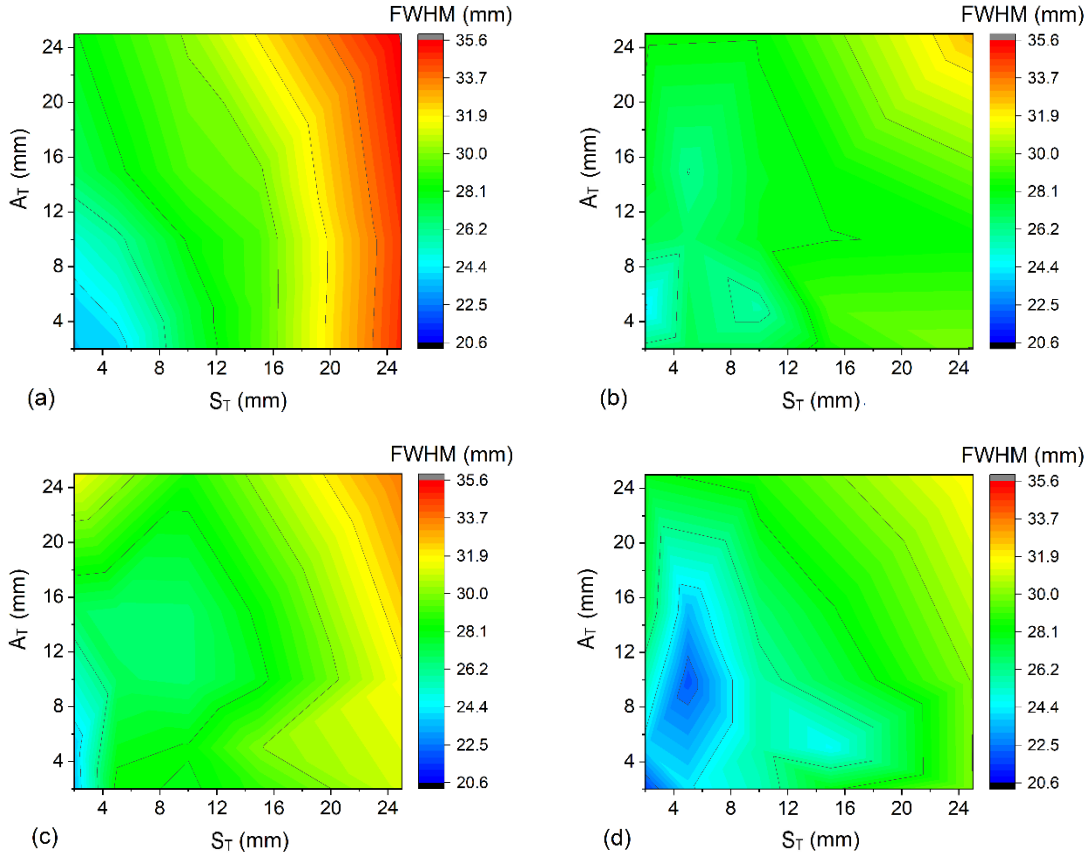

Figure 6. Spatial resolution (FWHM) function of the scatterer and absorber thickness for (a) 364, (b) 511, (c) 662, and (d) 1000 keV gamma-ray source from upper left to lower right, respectively. In the study, scatterer size and absorber sizes are $8 \cdot 8\,\mathrm{cm}^2$and $10 \cdot 10\,\mathrm{cm}^2$, respectively. The S_T and A_T pitch were both 5 mm.

of multiple scattering also increases in high S_T. Therefore, by increasing the S_T, the number of scattered photons reaching the absorber increases initially and then decreases due to complete absorption in the scatterer or escaping from the other side of the scatterer.

3.4 Geometric variable parameter: S_T and A_T, and SAD, constant parameters: S_A and A_A

Figure 8 and 9 show the influence of the SAD and detector thickness on the spatial resolution and the DE_a (%) of the CC, respectively. In the study, the scatterer thickness equals absorber thickness, and the scatterer and absorber area are $8 \cdot 8\,\mathrm{cm}^2$and $10 \cdot 10\,\mathrm{cm}^2$, respectively. There is a paradoxical effect between SAD and detector thickness on spatial resolution. In general, all studied energies show the same trends for spatial resolution so that it improved as the SAD increased in a certain thickness and degrade as the detector thickness increased in a particular SAD. The former and latter are due to reducing and increasing the uncertainty on the cone axis direction, respectively. In other words, the parallax error decreases and increases by increasing the SAD and detector thickness, respectively [32, 33]. The influence of the large SAD on the spatial resolution is significantly more pronounced than the influence of the detector thickness. Hence, the change range of spatial resolution is limited in long SAD ($>$ 30 mm) compared to low value SAD while increasing the detector thickness.

2023 JINST 18 P01035

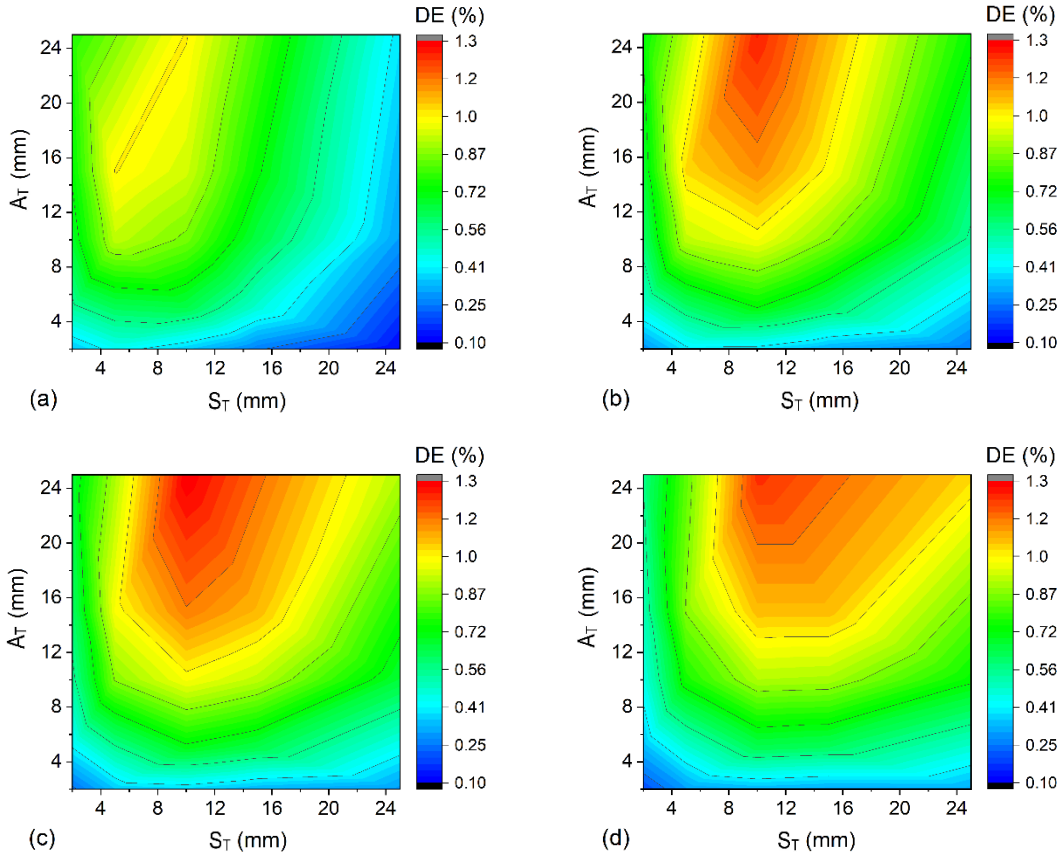

Figure 7. DE_a (%) is a function of scatterer thickness (S_T) and absorber thickness (A_T) for (a) 364, (b) 511, (c) 662, and (d) 1000 keV gamma-ray sources from the upper left to the lower right. The condition is the same as what is mentioned in figure 6.

The DE_a increase obviously by increasing detector thickness and decrease by SAD increment. The former and latter are due to the increasing probability of photon interaction with layers and the decreasing of the solid angle subtended by the absorber from the scatter detector.

4 Discussion

The GATE simulation results obtained in this study are reliable according to good agreement between experiment and simulation results reported in our previous work [15]. The DE_a and spatial resolution for the energy range, 364–1000 keV, showed almost the same trends. The spatial resolution generally is poor when the efficiency is high and vice versa. Our results show that the most important contributions to the camera's spatial resolution are SAD and scatterer area at the same changing ratio. The scatterer area and SAD also offer the most important contributions to the DE_a of the camera at the same changing ratio, respectively. Increasing SAD and scatterer area decreases DE_a and increases DE_a, respectively. In small SADs, the effect of scatterer area increment on DE_a growth is more significant than in large SAD cases.

2023 JINST 18 P01035

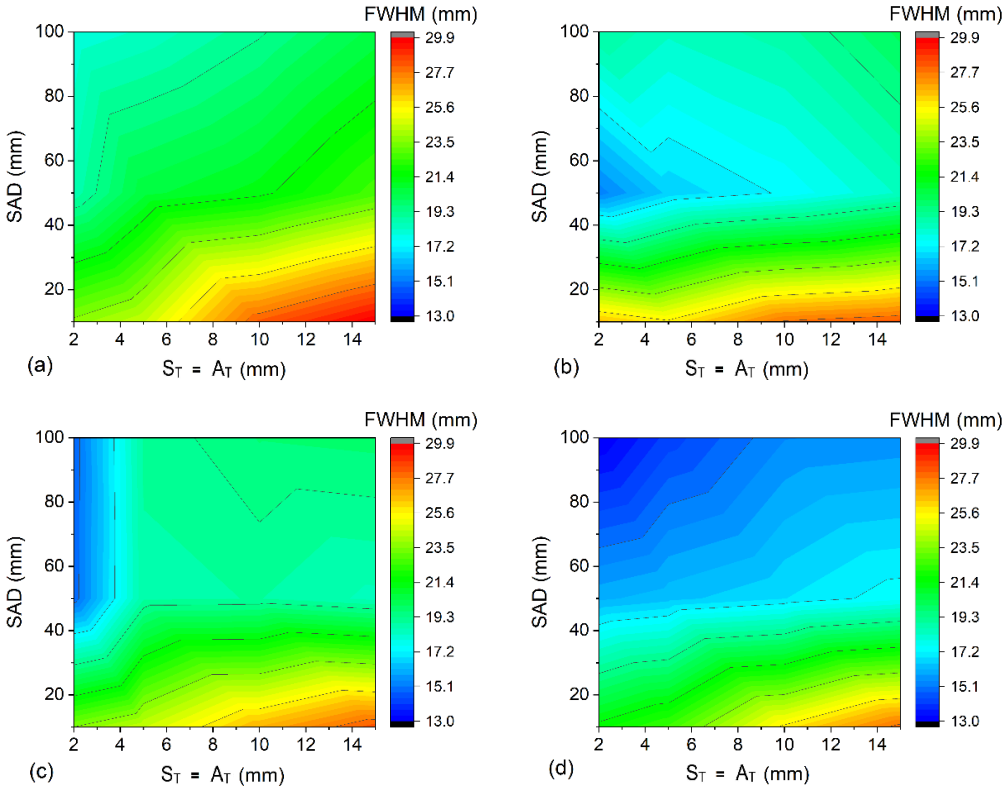

Figure 8. spatial resolution (FWHM) as a function of scatterer-absorber distance (SAD) and detector thickness (mm) for (a) 364, (b) 511, (c) 662, and (d) 1000 keV gamma-ray source from upper left to lower right, respectively. In the study, the scatterer thickness equals absorber thickness, and the scatterer and absorber area are $8 \cdot 8\,\mathrm{cm}^2$ and $10 \cdot 10\,\mathrm{cm}^2$, respectively. The S_T and A_T pitch were both 5 mm and the SAD was considered to be 10, 50 and 100 mm.

The S_A, compared to A_A, showed more influence on DE_a, while A_T, compared to S_T, showed more effect on DE_a. The former is due to a significant difference in subtended angles between the two layers. The latter is due to the importance of thickness on the probability of Compton and photoelectric occurrence. It is worth mentioning that by doubling the scatterer area, detection efficiency almost doubles; doubling absorber thickness increases detection efficiency lower than 1.5 times. Therefore, the scatterer area effect is greater than the absorber thickness on detection efficiency. Among the parameters, the changing in the absorber area (A_A) showed the most negligible impact on DE_a for all studied energies.

The changing in the SAD and absorber area (A_A) showed negligible impact on the spatial resolution for all studied energies. However, both parameters affect the range of subtended angles by absorber from scatterer as the exact mechanism. It is due to the absorber area equal to or greater than the scatterer area and the absorber's limited range of the subtended angles from the scatterer. Accordingly, the subtended angles by absorber from scatterer were not changed significantly by increasing the absorber area.

The results show that the dependency of considered parameters on the geometry characteristics of detectors is significantly reduced when the SAD increases. Imaging resolution and DE_a are

2023 JINST 18 P01035

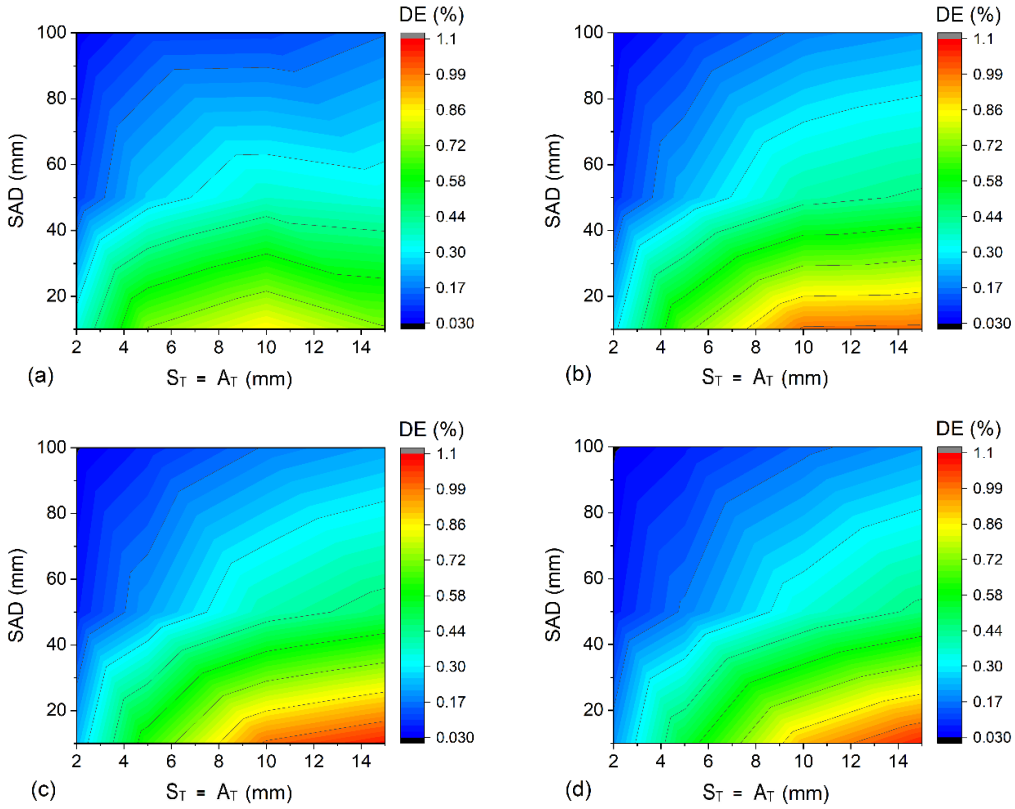

Figure 9. DE_a (%) as a function of scatterer-absorber distance (SAD) and detector thickness (mm) for (a) 364, (b) 511, (c) 662, and (d) 1000 keV gamma-ray sources from the upper left to the lower right, respectively. The condition is the same as what is mentioned in figure 8.

affected considerably by changing the detector's area and thickness in case of the short SAD. On the other hand, spatial resolution and DEa are significantly involved by changing the detector's size. They are less affected by the detector's thickness in case of the higher SAD (> 4 cm).

To increase DE_a without noticeable degrading spatial resolution when the SAD is fixed in small values (< 4 cm), the strategy is to increase the absorber's area or thickness. However, the latter has a more dominant effect. To improve imaging resolution without significant reduction of DE_a when the SAD is fixed in small values (< 4 cm), the strategy is the decreasing the scatterer's thickness.

Enlarging the detector's thickness against the area up to an optimized value increases DE_a without significant degrading spatial resolution while taking advantage of long SAD. This observation is because the detector's thickness increment enhances DE_a up to a maximum value, then DE_a decreases. When the other geometrical parameters are the same, the optimized thickness differs for different SADs.

Regarding the effect of energy on spatial resolution in the same geometry, it can be said that it improves with increasing energy. The improvement is not noticeable when the energy difference is negligible. But for energy 1000 keV, spatial resolution is significantly improved compared to low energy. The main reasons are the decrease of uncertainty induced by Doppler broadening in determining the energy of Compton scatters [34] and the increase of the energy resolution.

2023 JINST 18 P01035

5 Conclusions

This study investigated the impact of altering geometrical parameters on GAGG scintillator-based CC performance (DE_a and spatial resolution) for different source energies (364, 511, 662, and 1000 keV) by GATE Monte Carlo simulation. These parameters included the planner area of scatterer and absorber detectors, their thicknesses, and the distance between them. The DE_a and spatial resolution for the energy range, 364–1000 keV, showed almost the same trends which facilitate the construction of a particular CC in multi-color imaging. Although the value of CC's spatial resolution and DE_a will vary according to input parameters; energy resolution, intrinsic spatial resolution, time coincidence window, etc., the trends are expected to be maintained. The results showed that decreasing the scatterer area and increasing the SAD influence the improvement of CC's spatial resolution and vice versa for detection efficiency. The results show that the dependency of considered parameters on the geometrical characteristics of detectors is significantly reduced when the SAD increases. Considering the dimension of CC's component detectors and their distance, it is expected that it could be used as a portable CC. Much analysis of geometrical factors needs to be done before a CC is designed and finally becomes a viable instrument. The simulation study's findings presented here will provide valuable guidelines for researchers choosing a desired CC's design according to particular objectives, manufacturing limitations in scintillator growth, cost, etc.

Acknowledgments

The Program supported this work on the Open Innovation Platform with Enterprises, Research Institute, and Academia, Japan Science and Technology Agency (JST, OPERA, JPMJOP1721). This work was supported partly by JSPS KAKENHI Grant Numbers JP16K15351, JP18K14556, and JP21K15855. The authors gratefully acknowledge the use of the services, facilities, and excellent experimental conditions provided by the Cyclotron and Radioisotope Center (CYRIC), Tohoku University, Miyagi, Japan.

References

[1] R. Pani, R. Pellegrini, M.N. Cinti, C. Polito, C. Orlandi, A. Fabbri et al., *Integrated ultrasound and gamma imaging probe for medical diagnosis*, 2016 *JINST* **11** C03037.

[2] A. Lipovec, K. Shimazoe and H. Takahashi, *Development of high-resolution gamma detector using sub-mm GAGG crystals coupled to TSV-MPPC array*, 2016 *JINST* **11** C03026.

[3] R. Pani, A. Pergola, M. Bettiol, M. Longo, C. Polito, R. Falconi et al., *Characterization of monolithic GAGG:Ce coupled to both PMT and SiPM array for gamma imaging in Nuclear Medicine*, 2020 *JINST* **15** C05011.

[4] M. Uenomachi, M. Takahashi, K. Shimazoe, H. Takahashi, K. Kamada, T. Orita et al., *Simultaneous in vivo imaging with PET and SPECT tracers using a Compton-PET hybrid camera*, *Sci. Rep.* **11** (2021) 17933.

[5] M. Uenomachi, K. Shimazoe, K. Ogane and H. Takahashi, *Simultaneous multi-nuclide imaging via double-photon coincidence method with parallel hole collimators*, *Sci. Rep.* **11** (2021) 13330.

[6] A. Kishimoto, J. Kataoka, T. Taya, L. Tagawa, S. Mochizuki, S. Ohsuka et al., *First demonstration of multi-color 3-D in vivo imaging using ultra-compact Compton camera*, *Sci. Rep.* **7** (2017) 2110.

2023 JINST 18 P01035

[7] A. Omata, M. Masubuchi, N. Koshikawa, J. Kataoka, H. Kato, A. Toyoshima et al., *Multi-modal 3D imaging of radionuclides using multiple hybrid Compton cameras*, *Sci. Rep.* **12** (2022) 2546.

[8] H. Tashima and T. Yamaya, *Compton imaging for medical applications*, *Radiol. Phys. Technol.* **15** (2022) 187.

[9] Y. Suzuki, M. Yamaguchi, H. Odaka, H. Shimada, Y. Yoshida, K. Torikai et al., *Three-dimensional and multienergy gamma-ray simultaneous imaging by using a si/CdTe compton camera*, *Radiology* **267** (2013) 941.

[10] J.-P. Zhang, X. zuo Liang, J. le Cai, Y. Liu, X. chao Huang, D. wu Li et al., *Prototype of an array SiPM-based scintillator compton camera for radioactive materials detection*, *Radiat. Detect. Technol. Meth.* **3** (2019) 17.

[11] K. Shimazoe, M. Yoshino, Y. Ohshima, M. Uenomachi, K. Oogane, T. Orita et al., *Development of simultaneous PET and Compton imaging using GAGG-SiPM based pixel detectors*, *Nucl. Instrum. Meth. A* **954** (2020) 161499.

[12] K. Shimazoe et al., *Development of a Compton Camera based on digital SiPMs and GAGG crystals*, in *Proceedings of IEEE Nuclear Science Symposium and Medical Imaging Conference*, Seoul, Souh Korea, 27 October–2 November 2013, pp. 1–3.

[13] J.-X. Wen, X.-T. Zheng, J.-D. Yu, Y.-P. Che, D.-X. Yang, H.-Z. Gao et al., *Compact CubeSat Gamma-Ray Detector for GRID Mission*, *Nucl. Sci. Tech.* **32** (2021) 99 [arXiv:2104.14228].

[14] Y. Nagao, M. Yamaguchi, N. Kawachi and H. Watabe, *Development of a cost-effective Compton camera using a positron emission tomography data acquisition system*, *Nucl. Instrum. Meth. A* **912** (2018) 20.

[15] H. Zarei, Y. Nagao, K. Yamamoto, M. Itoh, M. Yamaguchi, N. Kawachi et al., *The performance study of developed cost-effective Compton Camera based on Ce:GAGG scintillator using experimental measurements and CCMod of GATE simulation module*, 2022 *JINST* **17** P10012.

[16] E. Yoshida, H. Tashima, K. Nagatsu, A.B. Tsuji, K. Kamada, K. Parodi et al., *Whole gamma imaging: a new concept of PET combined with Compton imaging*, *Phys. Med. Biol.* **65** (2020) 125013.

[17] A. Koyama, Y. Nakamura, K. Shimazoe, H. Takahashi and I. Sakuma, *Prototype of a single probe Compton camera for laparoscopic surgery*, *Nucl. Instrum. Meth. A* **845** (2017) 660.

[18] R.K. Parajuli, M. Sakai, W. Kada, K. Torikai, M. Kikuchi, K. Arakawa et al., *Annihilation gamma imaging for carbon ion beam range monitoring using Si/CdTe Compton camera*, *Phys. Med. Biol.* **64** (2019) 055003.

[19] S. Mochizuki, J. Kataoka, A. Koide, K. Fujieda, T. Maruhashi, T. Kurihara et al., *High-precision compton imaging of 4.4 MeV prompt gamma-ray toward an on-line monitor for proton therapy*, *Nucl. Instrum. Meth. A* **936** (2019) 43.

[20] Y. Nagao, M. Yamaguchi, S. Watanabe, N.S. Ishioka, N. Kawachi and H. Watabe, *Astatine-211 imaging by a compton camera for targeted radiotherapy*, *Appl. Radiat. Isot.* **139** (2018) 238.

[21] A. Omata, J. Kataoka, K. Fujieda, S. Sato, E. Kuriyama, H. Kato et al., *Performance demonstration of a hybrid Compton camera with an active pinhole for wide-band X-ray and gamma-ray imaging*, *Sci. Rep.* **10** (2020) 14064.

[22] K. Ogane, M. Uenomachi, K. Shimazoe, M. Takahashi, H. Takahashi, Y. Seto et al., *Simultaneous measurements of single gamma ray of 131i and annihilation radiation of 18f with compton PET hybrid camera*, *Appl. Radiat. Isot.* **176** (2021) 109864.

2023 JINST 18 P01035

[23] S. Jan et al., *GATE: A Simulation toolkit for PET and SPECT*, *Phys. Med. Biol.* **49** (2004) 4543 [physics/0408109] [INSPIRE].

[24] A. Etxebeste, D. Dauvergne, M. Fontana, J.M. Létang, G. Llosá, E. Munoz et al., *CCMod: a GATE module for compton camera imaging simulation*, *Phys. Med. Biol.* **65** (2020) 055004.

[25] L. Barrientos, M. Borja-Lloret, A. Etxebeste, E. Muñoz, J.F. Oliver, A. Ros et al., *Performance evaluation of MACACO II Compton camera*, *Nucl. Instrum. Meth. A* **1014** (2021) 165702.

[26] https://www.c-and-a.jp/assets/img/products/103210514_HR-GAGG.pdf.

[27] GEANT collaboration, *Guide For Physics Lists* (2020).

[28] https://root.cern/releases/release-62000/.

[29] R. Brun and F. Rademakers, *ROOT: An object oriented data analysis framework*, *Nucl. Instrum. Meth. A* **389** (1997) 81.

[30] O. Klein and Y. Nishina, *Über die Streuung von Strahlung durch freie Elektronen nach der neuen relativistischen Quantendynamik von Dirac*, *Zeit. Phys.* **52** (1929) 853.

[31] G.F. Knoll, *Radiation detection and measurement*, John Wiley & Sons (2010).

[32] Y. Calderón, *Design, development, and modeling of a compton camera tomographer based on room temperature solid statepixel detector*, Ph.D. thesis, Universitat Autònoma de Barcelona (2014).

[33] M.H. Richard, M. Dahoumane, D. Dauvergne, M. De Rydt, G. Dedes, N. Freud et al., *Design Study of the Absorber Detector of a Compton Camera for On-Line Control in Ion Beam Therapy*, *IEEE Trans. Nucl. Sci.* **59** (2012) 1850.

[34] A. Zoglauer and G. Kanbach, *Doppler broadening as a lower limit to the angular resolution of next-generation compton telescopes*, *Proc. SPIE* **4851** (2003) 1302.

2023 JINST 18 P01035